ADVANCING EARTH AND SPACE SCIENCE

Geophysical Research Letters

RESEARCH LETTER
10.1029/2020GL087372

Key Points:
- Forty-one open-ocean tsunamis were detected in the continuous 32-year bottom pressure record from Axial Seamount in the northeast Pacific
- The high fidelity of the data is attributable to its long duration-high temporal resolution and the low ambient noise of deep-sea records
- The maximum and root-mean-square tsunami amplitudes follow a power-law distribution reminiscent of the Gutenberg-Richter law for earthquakes

Supporting Information:
- Supporting Information S1

Correspondence to:
R. E. Thomson,
richard.thomson@dfo-mpo.gc.ca

Citation:
Fine, I. V., Thomson, R. E., Chadwick, W. W., Jr, & Fox, C. G. (2020). Toward a universal frequency of occurrence distribution for tsunamis: Statistical analysis of a 32-year bottom pressure record at axial seamount. *Geophysical Research Letters*, *47*, e2020GL087372. https://doi.org/10.1029/2020GL087372

Received 3 FEB 2020
Accepted 11 APR 2020
Accepted article online 17 APR 2020

Toward a Universal Frequency of Occurrence Distribution for Tsunamis: Statistical Analysis of a 32-Year Bottom Pressure Record at Axial Seamount

Isaac V. Fine[1], Richard E. Thomson[1], William W. Chadwick Jr[2], and Christopher G. Fox[3]

[1]Fisheries and Oceans Canada, Institute of Ocean Sciences, Sidney, British Columbia, Canada, [2]Oregon State University, Cooperative Institute for Marine Resources Studies (CIMRS), Newport, OR, USA, [3]National Oceanic and Atmospheric Administration, Pacific Marine Environmental Laboratory, Newport, OR, USA

Abstract Detailed examination of a 32-year record of high-resolution bottom pressure measurements at Axial Seamount (and vicinity) in the northeast Pacific identified a total of 41 tsunamis between 1986 and 2018. All of the events were associated with tsunamigenic earthquakes with magnitudes of 7.0 and greater. Statistical analysis of the data reveals that the time series of maximum tsunami amplitude and root-mean-square (RMS) tsunami amplitude follow strict power-law distributions, with considerably less deviation than for coastal tide gauge records. The high statistical reliability of the seamount record is attributable to the long duration of the observations and to the low signal-to-noise ratio of digital open-ocean bottom pressure records. The power law for the RMS tsunami amplitude is especially stable and follows a pure Pareto distribution (with exponent, $\beta = 1.24$) even when the minimum threshold is increased to the point that only a few events remain in the time series.

Plain Language Summary We use a unique 32-year time series of nearly continuous bottom pressure measurements near the summit of an active submarine volcano (Axial Seamount) to determine the amplitudes of all tsunamis (big and small) that occurred in the Pacific Ocean between 1986 and 2018. The data were then used to derive an empirical power-law relationship between the "size" (amplitude) of the tsunami waves and their frequency of occurrence. Derivation of the power-law provides a major step toward the establishment of a tsunami size-frequency law equivalent to the Gutenberg-Richter law for earthquake magnitude.

1. Introduction

The determination of observation-based (empirical) relationships between the "size" of a geophysical processes and its frequency of occurrence is a fundamental goal of many branches of earth science. A well-known example is the power-law frequency distribution for earthquake magnitude, which began with the publication of the Gutenberg-Richter law in the middle of the last century (Gutenberg & Richter, 1944) and continues today as seismologists seek to include ever smaller events in the functional relationship (Ross et al., 2019). Although power law relationships have been derived for tsunamis (e.g., Burroughs & Tebbens, 2005; Geist & Parsons, 2006, 2011), formulation of statistical relationships has been limited by both the rarity of the events and the lack of long-term, high resolution tsunami records.

Prior to the mid-20th century, there were few tide gauge stations compared to earthquake measurement sites. Until the installation of 6-minute sampling Analog-to-Digital-Recording (ADR) tide gauges in the late 1960s and early 1970s, most coastal gauges recorded at hourly intervals. Because tsunamis typically have periods shorter than 1 hr and amplitudes less than ~10–20 cm, they were generally difficult to identify in the presence of ambient noise. In addition, tsunami archives typically only span a few decades, which are not sufficiently long to accurately determine the rate of occurrence for the largest tsunamis (Geist et al., 2009). In contrast to coastal tide gauge observations, tsunami measurements in the open ocean have always been measured in digital form by bottom pressure recorders (BPRs), known for their high signal-to-noise ratios. Moreover, coastal records are affected by site-specific resonant effects over spatial scales of several kilometers or less, whereas open-ocean BPR records are characteristic of much larger oceanic regions.

Bottom pressure measurements of long ocean waves started in the mid-1960s (Snodgrass, 1969). However, it was not until 1979 that the first record of an open-ocean tsunami was obtained (Filloux, 1982). Dozens of BPRs are now deployed throughout the World Ocean as part of regional tsunami warning systems (Rabinovich & Eblé, 2015). Based on research at NOAA's Pacific Marine Environment Laboratory in Seattle, a reliable deep-ocean BPR capable of recording high-quality tsunami waves was first deployed in the northeast Pacific in 1986 (Eblé & González, 1991). For almost every year, from the late 1980s to the present, autonomous BPRs have been moored within the ~1,500 m deep caldera of Axial Seamount off the coast of Oregon (Figure 1). The primary motivation of these deployments was to monitor vertical movements of the seafloor at this active volcano (Chadwick et al., 2013; Embley et al., 1999; Embley & Baker, 1999). These early BPRs recorded internally, so that data could only be retrieved upon instrument recovery (Chadwick et al., 2006; Chadwick et al., 2012; Fox, 1990, 1999; Nooner & Chadwick, 2009; Nooner & Chadwick, 2016). In 1996, before the undersea volcanic eruption at Axial Seamount in January 1998, the New Millennium Observatory Project (NeMO) was established to start long-term monitoring at the site (Hammond et al., 2015). Beginning in 2014, additional BPRs were deployed at Axial Seamount as part of the Ocean Observatories Initiative (OOI) Cabled Array (Cowles et al., 2010; Kelley et al., 2014), which presently connects four BPRs and other instruments in real-time through an optical cable to a station at Pacific City, Oregon (Figure 1). The high quality BPR records from Axial Seamount starting in 1986, combined with more recent BPR records from neighboring buoys and cabled stations, constitute one of the longest BPR records for tsunami research in the ocean.

The purpose of this study was to use the nearly continuous 32-year record of bottom pressure at Axial Seamount to establish a precise size-frequency relationship for global tsunamis. Small gaps in the seamount record have been filled by data from nearby BPR sites. The results from our analysis of the tsunami waves recorded at the seamount provide a major step toward meeting our intended goal.

2. Observations

This study uses the records from 35 individual BPR deployments available for Axial Seamount and vicinity (Chadwick & Nooner, 2015; Fox, 2016), as well as four records from the Cleft Segment of Juan de Fuca Ridge, located roughly 100 km to the south (Figure 1) and recent 2016–2018 data from the OOI. Tsunami records from Axial Seamount and the Cleft Segment for the Mariana Trench event of 8 August 1993 (the only tsunami to be recorded simultaneously at the two sites) provided a wave variance ratio (Axial/Cleft) of 1.17. This ratio was then used to scale-up the variance of 0.65 mm^2 obtained for the Cleft Segment during the Kermadec Islands tsunami of 20 October 1986 (the only tsunami observed at the Cleft Segment but not at Axial Seamount) to a value of 0.76 mm^2 for the seamount. A similar analysis was performed for the peak amplitude values. Because both events were weak, neither was used in the statistical analysis. The combined BPR records for Axial Seamount span the 32.4-year period from 20 October 1986 to 31 December 2018, with approximately 4.4 years of cumulative gaps. Only one significant tsunami, the Cape Mendocino tsunami of 25 April 1992 (González et al., 1995), was missed due to the gaps. Because the quality of the data is generally high, it was possible to use all available records in the tsunami analyses. Records from 1986–1992 are at 56.25-s sampling intervals, while all other records are at intervals of 15 s or shorter.

3. Methods

A sequence of steps was taken to extract the tsunami waves from the bottom pressure records:

1. We first determined the times and locations of possible tsunamigenic earthquakes in the North Pacific; that is, those that occurred off Japan, Alaska, Russia, and North America and were known to have generated at least a local tsunami (NCEI Global Tsunami Database, NGDC, 2019). For each of 122 earthquakes identified, we computed the long wave travel time from the earthquake location to the BPR site using the method of Fine and Thomson (2013). Based on Huygens Principle, the method uses an eight-grid point pattern and the most recent data on the advancing tsunami wavefront orientation to calculate the time for the waves to travel to a specific location. Although the assumptions used in the method are not fully valid for very long

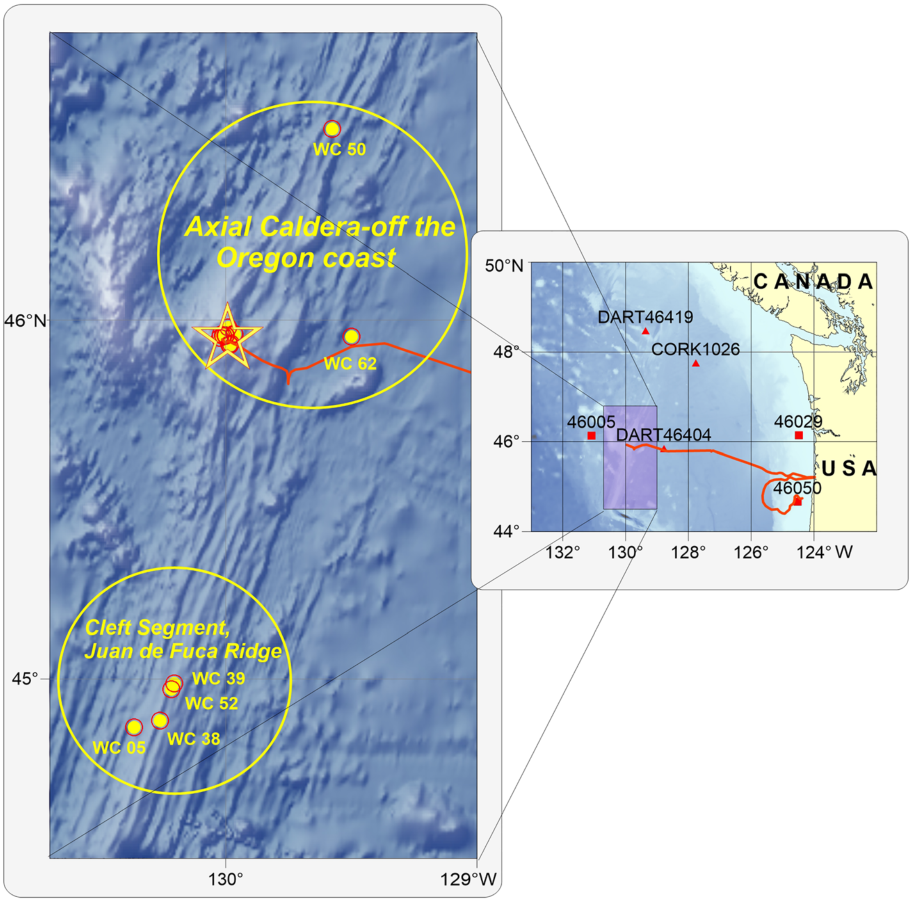

Figure 1. Locations of bottom pressure recorders (BPRs) at Axial Seamount and vicinity. The star marks the Axial Seamount summit where most BPR data were collected; WC 50 and WC 62 show locations of early BPR measurement sites to the north and east. Also shown are locations of BPRs at the Cleft Segment, offshore DART sites and CORK 1026 of the Ocean Drilling Program (ODP). Sites 46029 and 46050 are coastal weather buoys. Lines denoting the OOI Cabled Observatory terminate in Pacific City, Oregon.

source-site separations, the difference from actual arrival times for most tsunamis did not exceed a few percent.

To distinguish the tsunami signal from background noise, we used the frequency (*f*) versus time (*t*) wavelet approach developed by González and Kulikov (1993). Because of dispersive wave effects, the higher frequency waves from an earthquake arrive later than lower frequency waves. This effect is recognizable in a wavelet *f*-*t* diagram, when compared to the theoretical arrival curve. To estimate the theoretical arrival curve, an effective depth, H_e, along the tsunami ray path is first calculated. This depth is computed as that for an ocean of constant depth, H_e, for which the travel time along the ray path is the same as that for the long-wave travel time based on the actual bathymetry.

A ray path is calculated using two computed wave travel time maps: one from the earthquake location, $t(\lambda_E, \phi_E, \lambda, \phi)$, and the other from the BPR location, $t(\lambda_0, \phi_o, \lambda, \phi)$. Here, λ,ϕ are longitude and latitude, and subscripts *E* and *0* apply to the earthquake and BPR locations, respectively. The ray path, $\rho(\lambda, \phi)$, is computed as a set of points for which the sum of these two travel times is a minimum. We then compute the arrival time for each of the earthquake events as

$$T_A(\omega) = T_E + t_0(\lambda_E, \phi_E)\frac{\sqrt{gH_e}}{c_g(\omega, H_e)}, \qquad (1)$$

where T_E is the time of the earthquake, $t_0(\lambda_E, \phi_E) = t(\lambda_E, \phi_E, \lambda_0, \phi_0)$ is a long wave travel time from the source to the BPR location, and H_e is the effective depth computed using the length of the ray path, R, and travel time, t. Here,

$$H_e = \frac{1}{g}\left[\frac{R(\lambda_E, \phi_E)}{t_0(\lambda_E, \phi_E)}\right]^2, \tag{2}$$

where g is the gravitational acceleration and $c_g(\omega; H_e)$ is the group speed for a wave with an angular frequency ω,

$$c_g = \frac{1}{2}c\left[1 + \frac{2kH_e}{\sinh(2kH_e)}\right], \tag{3a}$$

where c is the phase speed,

$$c = \sqrt{\frac{g}{k}\tanh(kH_e)}, \tag{3b}$$

and k is the wavenumber.

2. The data were interpolated, where necessary, to a uniformly spaced time series with a 15-s sampling interval, de-tided using harmonic analysis (Pawlowicz et al., 2002), and then filtered using a tsunami-band filter with cut-off periods of 3 and 120 min.

3. For each event, we extracted a 2-day subset of the time series centered at the theoretical arrival time of the tsunamis. A Morlet wavelet analysis (e.g., Thomson & Emery, 2014) was then applied to the 2-day records to determine the tsunami wave forms as functions of frequency and time. The dispersion-dependent theoretical arrival time was incorporated in the wavelet plots to confirm, visually, the presence of a tsunami. For many of the events, there were two or more BPR records contributing to the pool of wavelet diagrams.

4. Results

We analyzed 230 wavelet diagrams spanning 122 earthquakes catalogued for the Pacific Ocean over the period 1986–2018 in the NCEI Global Tsunami Database (NGDC, 2019). Ninety-one of the diagrams contained tsunami waves from 41 earthquakes, all of which had magnitudes of 7.0 or greater. Figure 2a shows the time lines of the available BPR data, together with the names of 11 well-studied tsunamigenic earthquakes around the Pacific (detailed information on the 91 tsunami records is presented in Tables S1 and S2 of the supporting information).

Figure 2b shows the locations of the 41 earthquake sources for the tsunamis recorded at Axial Seamount, along with the wave ray paths from the source to the seamount. The ray paths represent the shortest computed travel time for the waves. While the trace for the shortest time does not necessarily coincide with the actual trajectory of the most energetic tsunami waves, the trajectories are identical, or nearly identical, for many of the tsunami source regions. For example, all tsunamis that originated near Japan, the Kuril Islands, Kamchatka, or the Aleutian Islands (a total of 12 events) had the same path. Also, events from northern Chile and Peru had the same paths, while those from central and southern Chile had slightly different paths. For tsunamis following a given trajectory, the wave transformation along a ray will be similar. Consequently, it is possible to forecast the effect of a specific tsunami originating from a source located near a historical source, not only for Axial Seamount but also for neighboring locations along the British Columbia-Washington-Oregon coast.

4.1. Detection of Tsunami Events: Specific Examples

The Kuril Island tsunami of 13 January 2007, generated by a strong $M_w = 8.1$ deep-water earthquake (Lobkovsky et al., 2009), provides an example of a well-defined tsunami record at Axial Seamount. Tsunami waves from the event are evident in the time series of the de-tided BPR record (upper pane in Figure 3a) and even more well-defined in the wavelet diagram (lower pane in Figure 3a). The waves from this event were in the 2 to 30 cph frequency band (periods of 30 to 2 min), and the leading waves were clearly dispersive. Another clear example is the record from the Irian-Jaya tsunami generated by the strong (M_w 8.2)

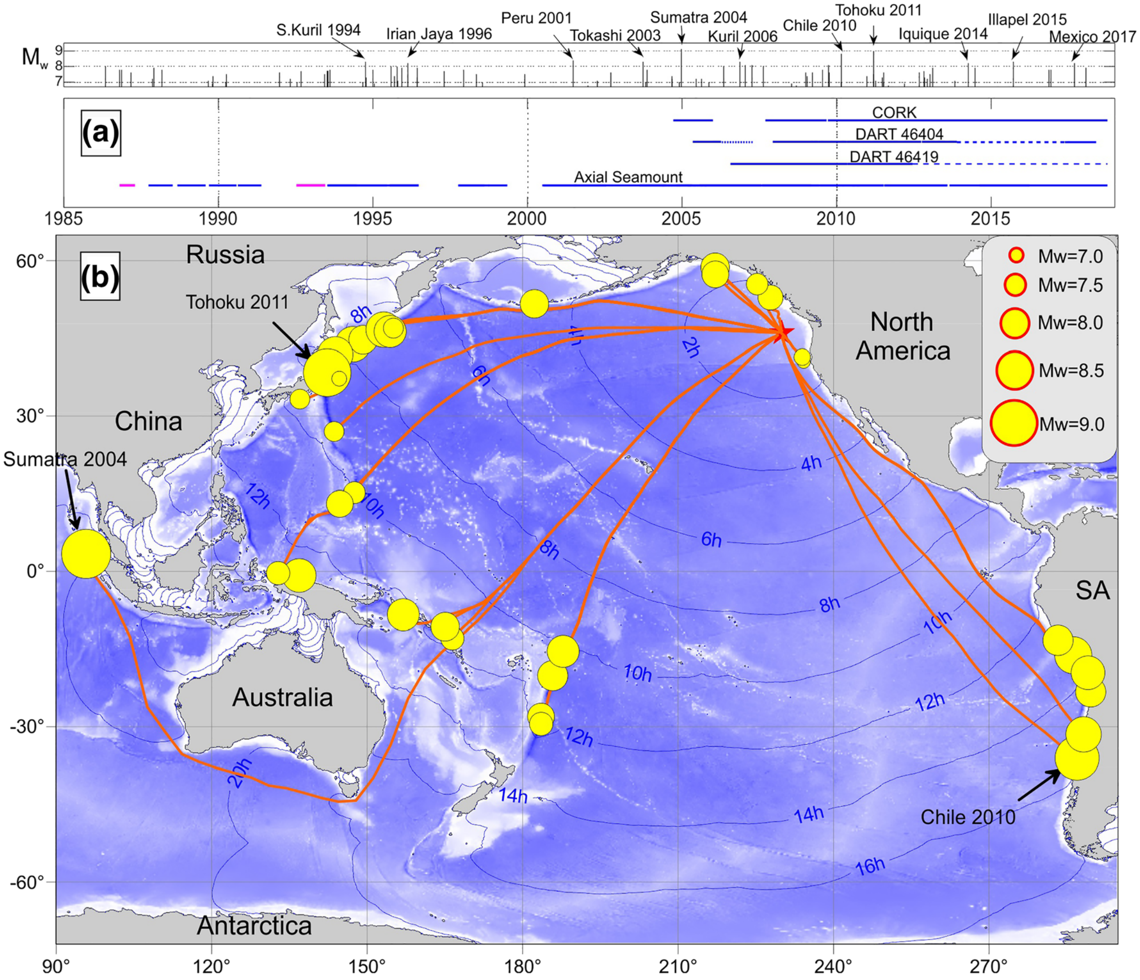

Figure 2. Temporal coverage of the BPR records and observed tsunamis at Axial Seamount and vicinity for 1986–2018. (a) Times of earthquakes and their magnitudes (M_W), along with periods spanned by the BPR series at Axial Seamount and the nearby CORK and DART sites 446404 and 46419 (see Figure 1 for location). The magenta segments on the Axial Seamount time-line indicate recordings at Cleft Segment; the dashed lines denote time intervals for which continuous records are not available; and (b) source regions for the tsunamis recorded at Axial Seamount. Earthquake magnitudes are proportional to circle areas. Thick red lines denote the ray traces (computed as having minimum propagation times) from the earthquake location to Axial Seamount; thin blue lines denote isochrones, marking the leading edge of the tsunami at 2-hr intervals after the initial earthquake.

earthquake in the Irian Sea on 17 February 1996 (Imamura et al., 1997). Based on the wavelet diagram (Figure 3b) for this poorly studied event, we find than the tsunami spanned a much lower frequency band than the Kuril Island 2007 event, which is attributable to the shallow water in the Irian-Jaya tsunami source region.

The short frontal wave of the Mendocino Ridge tsunami of 1 September 1994 (M_W 7.0) exemplifies tsunami waves originating with a near-field source. Although this was a low energy tsunami, the 4 mm wave amplitudes are readily detectable in the wavelet analysis because of the low background noise at the time (Figure 3c). There were no secondary waves in the record or in the wavelet diagram because of the weak source and close proximity to the seamount. We know of no other recordings of this tsunami except for the small waves reported for Crescent City (Lander et al., 2003). Our analysis also identified another weak near-field tsunami associated with the Northern California earthquake of 15 June 2005 ($M_w = 7.2$).

The BPR record from the Rat Islands tsunami of 17 November 2003 is an example of a poorly defined tsunami. As indicated by the time series and wavelet diagram in Figure 3d, the background noise was extremely high because of the strong storm on 17 November off the Oregon-Washington coast. Meteorological observations from nearby stations reveal high sea conditions around this date, with a maximum significant wind

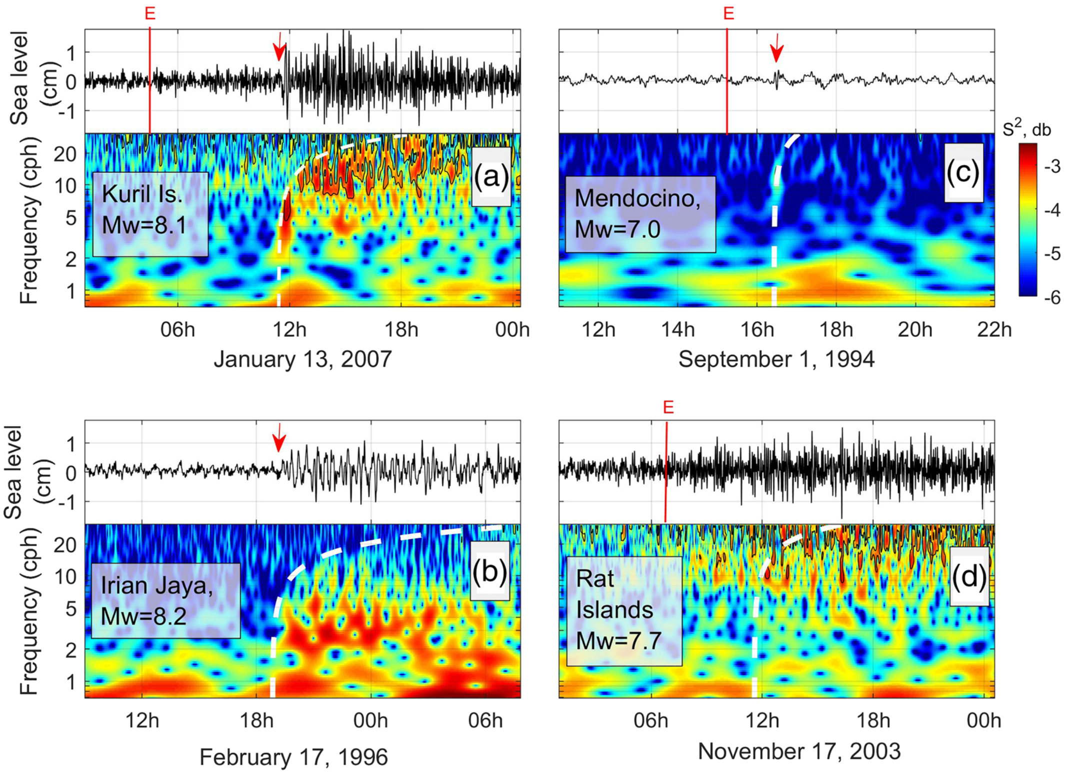

Figure 3. Anomalies of bottom pressure variations (converted to an equivalent sea level height) for selected tsunamis recorded at Axial Seamount, together with their corresponding wavelet diagrams. Times in UTC. (a) The 13 January 2007 Kuril Islands tsunami; (b) the 17 February 1996 Irian-Jaya tsunami; (c) the 1 September 1994 Mendocino Ridge tsunami; and (d) the 17 November 2003 Rat Islands tsunami. Bottom pressure anomalies were obtained by removing the tides. Red arrows denote the observed tsunami arrival time, the letter "E" and red line indicate the time of the earthquake. The dashed white lines in the wavelet diagrams denote the theoretical tsunami arrival times. The letter "E" is missing from (b) because the earthquake occurred off Indonesia well before the time period covered by the plot.

wave height of 11.3 m in the morning of 17 November at buoy 46005, located roughly 80 km to the west of Axial Seamount (Figure 1). Significant wave heights of 8–9 m were recorded later in the day at coastal buoys 46029 and 46050.

According to the data and numerical simulations (Rat Islands Tsunami, 2019), most of the energy from the Rat Islands event went to the south toward the Hawaiian Islands, with little energy propagating to the east, where open ocean tsunami amplitudes were predicted to be only a few millimeters. Such small waves are impossible to detect during times of high background noise, as occurred at Axial Seamount at this time. We have characterized this event as "non-detectable" and do not include it in our study (Table S1).

4.2. Statistical Analysis

Both the variance and maximum wave amplitude are characteristics of tsunami strength and can be used as the "size" parameter when estimating a sortable statistic of tsunami events (Geist & Parsons, 2006). As with other natural hazards, the frequency-size distribution for tsunamis at a particular location tends to follow a power-law relationship or a pure Pareto distribution (Burroughs & Tebbens, 2005) of the form,

$$\Phi(R) = \left(\frac{R_{\min}}{R}\right)^{\beta}, \tag{4}$$

where $\Phi(R) = 1 - F(R)$ is the survival function obtained from the cumulative distribution function, $F(R)$. Here, R is the size of a tsunami (either tsunami amplitude or variance), R_{min} is the smallest size value for which the power law holds, and β is the shape parameter, or in the case of the Pareto distribution, the power-law exponent.

To estimate β, we use the maximum likelihood estimate (Kagan, 2002), yielding

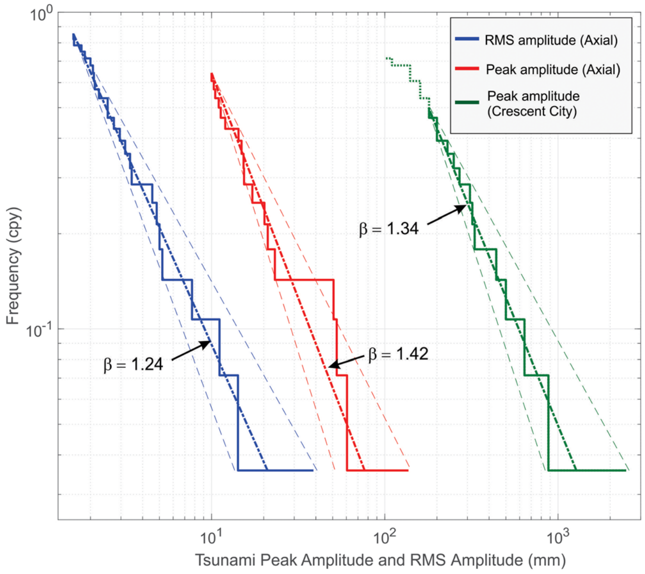

Figure 4. Cumulative distributions, $F(R)$, and power-law exponents for tsunamis recorded at Axial Seamount during 1986–2018 based on: (1) the RMS wave amplitude records for the 24 highest tsunamis (blue line); (2) the maximum wave amplitude for the highest 18 tsunamis (red line); and (3) the maximum wave amplitudes for the highest 15 events at Crescent City, California. The frequency axis is in cycles per year (cpy). Thick dashed lines denote the Pareto power-law distributions with specified shape parameters; thin dashed lines span the ±1 standard error confidence intervals.

$$\frac{1}{\widehat{\beta}} = \frac{1}{N}\sum_{i=1}^{N}\frac{R_i}{R_{\min}}, \tag{5}$$

where N is the number of observations. We have used two types of variables to characterize the intensity of tsunamis at Axial Seamount: (1) The maximum tsunami amplitude for each event and (2) the square root of the variance (i.e., the root-mean-square [RMS] amplitude) for the first 12 hr of the tsunami wave record. If there are several records for a specific tsunami, we computed the mean value of the wave amplitude variable. We then determined the thresholds for the two types of statistics. Based on our ability to detect tsunami waves within the sometimes noisy BPR records (as discussed in the previous section), we choose 1 cm as the minimal tsunami amplitude and 1.5 mm as the minimum tsunami RMS amplitude. A total of 18 events had tsunami amplitudes in excess of 1 cm, and 24 events had RMS amplitudes in excess of 1.5 mm.

As indicated by Figure 4, the tsunami distribution based on the RMS estimates has a marked power-law dependence, with $\beta = 1.24$ for the full set of 24 events, with small variability around this value depending on the threshold. Even for a high threshold of 8 mm, comprising only three tsunami events, the MLE estimation of the power parameter β remains close to that for the full set. We find no indication that the calculated distribution deviates from a power-law, even for the very largest events. On a strictly physical basis, the power-law must have a limitation, as tsunami size is limited by a number of factors, including the magnitude and extent of the earthquake source. Although such a limitation would normally lead to a truncated or a tapered Pareto distribution, there is no indication of this limitation for the Axial Seamount records. Perhaps, the 32-year open ocean record is too short to capture a change at the upper limit of the tsunami statistics. The beta parameter for the RMS statistics is greater than 1, which indicates that this statistic does not fall into the "heavy" category (Geist & Parsons, 2006). If β is less than 1, the distribution is considered "heavy" and has infinite statistical moments; otherwise, the statistical moments remain finite. Here, β is well above 1 for both the RMS amplitude and peak amplitude datasets. This result differs from Geist and Parsons (2006) who compute statistics for the Miako (Japan) tide gauge station, for which β equals 1.01 when the 2011 Tohoku event is included, and 1.09 when the event is excluded.

To compare estimates of β obtained for Axial Seamount with those for the nearby coast, we examined the tsunami statistics for several tide gauge stations on the west coasts of the United States and Canada using the Global Tsunami Database (NGDC, 2019). A majority of the tide gauge records have incomplete tsunami data sets with fewer than 10 tsunami events or had events that were too weak to include in the analysis. The primary exception is Crescent City, which is known to have high tsunami sensitivity and to have experienced serious damage from several events, including the 2006 Kuril Islands tsunami (Kowalik et al., 2008) and the 2011 Tohoku tsunami (Allan et al., 2012). As a result of this sensitivity, the tide gauge Crescent City provides a reliable coastal tsunami record compatible to that for Axial Seamount. Despite major differences in tsunami wave heights between the two sites, the statistical distributions in Figure 4 are similar. Although the shape parameter for Crescent City varies more as a function of the number of events and the selected threshold value than for Axial Seamount, it is still in the range of values derived for the seamount. Thus, our tsunami statistics are representative of this part of Pacific Ocean, which is open to distant tsunamis but not strongly affected by nearfield tsunamis, as is the case for the region off Japan.

5. Conclusions

This study analyzes 41 tsunamis identified in the long-term bottom pressure records at Axial Seamount and from nearby sites in the northeast Pacific. Many of the tsunamis were simultaneously recorded by up to six BPRs, and many of the records, especially those during the last two decades of the last century, appear to have been unknown to previous researchers. Statistical analysis of the tsunamis measured by the BPRs shows that the maximum wave amplitudes follow a strict power law distribution, having considerably less deviation than for coastal tide gauge records. The improved statistical reliability provided by the nearly continuous 32-year seamount record is attributed to the long duration of the digital observations and to the high fidelity (low signal-to-noise ratio) of the data series. The power law distribution derived from the RMS time series is remarkably stable, following a pure Pareto distribution up to the highest possible minimum threshold, when only a few events remain in the time series. That both the RMS and maximum amplitudes follow similar power-law distributions is, perhaps, not unexpected considering the statistical relationship between the two variables for a fully random processes (Cartwright & Longuet-Higgins, 1956). It is less clear why such a relationship would hold for impulsively generated tsunami waves not composed of a superposition of a large number of sinusoids with random phases.

The importance of our findings lies in the fact that open-ocean tsunami records contain mostly progressive waves, whereby the variance (and thus the RMS) of the wave heights characterize the “raw” energy flux that eventually impacts the adjoining coastal regions. The RMS statistics reflect the general statistical features for the entire coast, which then can be adjusted to specific locations using empirical and numerically simulated transfer functions between the bottom pressure records at the open ocean sites and the tide gauge records at coastal locations. This work also shows the value of long-term continuous BPR observations, which should continue at Axial Seamount for several more decades because of the Ocean Observatories Initiative Cabled Array infrastructure.

Acknowledgments

We are grateful to the editor and the two anonymous reviewers for their positive comments and suggestions. The pre-1998 BPR data are available on the NOAA-NCEI website: https://www.ngdc.noaa.gov/nndc/struts/results?&t=102597&s=1&d=1; the OOI BPR data are on the OOI Data Portal: https://oceanobservatories.org/data-portal/. See also the NOAA BPR archive, https://www.ngdc.noaa.gov/hazard/bpr/), as well as Chadwick & Nooner (2015) and Fox (2016) . The NOAA/PMEL Engineering Development Division provided invaluable support in collecting the BPR time-series in the NE Pacific.

References

Allan, J. C., Komar, P. D., Ruggiero, P., & Witter, R. (2012). The March 2011 Tōhoku tsunami and its impacts along the U.S. West Coast. *Journal of Coastal Research*, *28*(5), 1142–1153. https://doi.org/10.2112/JCOASTRES-D-11-00115.1

Burroughs, S. M., & Tebbens, S. F. (2005). Power law scaling and probabilistic forecasting of tsunami runup heights. *Pure and Applied Geophysics*, *162*, 331–342.

Cartwright, D. E., & Longuet-Higgins, M. S. (1956). The statistical distribution of the maxima of a random function. *Proceedings of the Royal Society of London. Series A. Mathematical and Physical Sciences*, *237*(1209), 212–232.

Chadwick, W., & Nooner, S. (2015). Processed Bottom Pressure Recorder (BPR) Data from Uncabled Instruments Deployed at Axial Seamount on the Juan de Fuca Ridge (Investigators William Chadwick and Scott Nooner). Integrated Earth Data Applications (IEDA), Marine Geoscience Data System, doi: https://doi.org/10.1594/IEDA/322282.

Chadwick, W. W. Jr., Clague, D. A., Embley, R. W., Perfit, M. R., Butterfield, D. A., Caress, D. W., et al. (2013). The 1998 eruption of axial seamount: New insights on submarine lava flow emplacement from high-resolution mapping. *Geochemistry, Geophysics, Geosystems*, *14*, 3939–3968. https://doi.org/10.1002/ggge20202

Chadwick, W. W. Jr., Nooner, S., Zumberge, M., Embley, R. W., & Fox, C. G. (2006). Vertical deformation monitoring at axial seamount since its 1998 eruption using deep-sea pressure sensors. *Journal of Volcanology and Geothermal Research*, *150*, 313–327. https://doi.org/10.1016/j.jvolgeores.2005.07.006

Chadwick, W. W. Jr., Nooner, S. L., Butterfield, D. A., & Lilley, M. D. (2012). Seafloor deformation and forecasts of the April 2011 eruption at axial seamount. *Nature Geoscience*, *5*(7), 474–477. https://doi.org/10.1038/NGEO1464

Cowles, T., Delaney, J., Orcat, J., & Weller, R. (2010). The ocean observatory initiative: Sustained ocean observing across a range of spatial scales. *Marine Technology Society Journal*, *44*, 54–64. https://doi.org/10.4031/MTSJ.44.6.21

Eblé, M. C., & González, F. I. (1991). Deep-ocean bottom pressure measurements in the Northeast Pacific. *Journal of Atmospheric and Oceanic Technology*, *8*(2), 221–233. https://doi.org/10.1175/1520-0426(1991)008<0221:DOBPMI>2.0.CO;2

Embley, R. W., & Baker, E. T. (1999). Interdisciplinary group explores seafloor eruption with remotely operated vehicle. *Eos, Transactions, American Geophysical Union*, *80*(19). https://doi.org/10.1029/99EO00157

Embley, R. W., Chadwick, W. W. Jr., Clague, D., & Stakes, D. (1999). The 1998 eruption of axial volcano: Multibeam anomalies and seafloor observations. *Geophysical Research Letters*, *26*(23), 3425–2428. https://doi.org/10.1029/1999GL002328

Filloux, J. H. (1982). Tsunami recorded on the open ocean floor. *Geophysical Research Letters*, *9*(1), 25–28. https://doi.org/10.1029/GL009i001p00025

Fine, I. V., & Thomson, R. E. (2013). A wavefront orientation method for precise numerical determination of tsunami travel time. *Natural Hazards and Earth System Sciences*, *13*, 2863–2870. https://doi.org/10.5194/nhess-13-22863-2013

Fox, C. G. (1990). Evidence of active ground deformation on the mid-ocean ridge: Axial seamount, Juan de Fuca Ridge, April-June, 1988. *Journal of Geophysical Research*, *95*, 12,813–12,822. https://doi.org/10.1029/JB095iB08p12813

Fox, C. G. (1999). In situ ground deformation measurements from the summit of Axial Volcano during the 1998 volcanic episode. *Geophysical Research Letters*, *26*(23), 3437–3440. https://doi.org/10.1029/1999GL900491

Fox, C. G. (2016). Processed Bottom Pressure Recorder (BPR) Data from Uncabled instruments deployed at Axial Seamount on the Juan de Fuca Ridge (investigator Chris Fox). Integrated Earth Data Applications (IEDA). https://doi.org/10.1594/IEDA/322344

Geist, E. L., & Parsons, T. (2006). Probabilistic analysis of tsunami hazards. *Natural Hazards*, *37*(2), 77–314. https://doi.org/10.1007/s11069-005-4646-z

Geist, E. L., & Parsons, T. (2011). Assessing historical rate changes in global tsunami occurrence. *Geophysical Journal International.*, *187*, 497–509. https://doi.org/10.1111/j.1365-246X.2011.05160.x

Geist, E. L., Parsons, T., ten Brink, U., & Lee, H. J. (2009). *Tsunami probability, in: The Sea*, v. 15: (pp. 93–135). Harvard University press, Cambridge, Massachusetts, USA.

González, F. I., & Kulikov, E. A. (1993). Tsunami dispersion observed in the deep ocean. In S. Tinti (Ed.), *Tsunamis in the World* (pp. 7–16). Dordrecht: Kluwer Acad. Publ.

González, F. I., Satake, K., Boss, E. F., & Mofjeld, H. O. (1995). Edge wave and non-trapped modes of the 25 April 1992 Cape Mendocino tsunami. *Pure and Applied Geophysics*, *144*, 409–426. https://doi.org/10.1007/BF00874375

Gutenberg, B., & Richter, C. F. (1944). Frequency of earthquakes in California. *Bulletin of the Seismological Society of America*, *34*, 185–188.

Hammond, S. R., Embley, R. W., & Baker, E. T. (2015). The NOAA Vents Program 1983 to 2013, Thirty years of ocean exploration and research. *Oceanography*, *28*(1), 160–173. https://doi.10.5670/oceanog.2015.17

Imamura, F., Subandono, G., Watson, A., Moore, T., Takahasji, H., Matsutomi, H., & Hidayat, R. (1997). Irian Jaya earthquake and tsunami cause serious damage. *Eos, Transactions American Geophysical Union*, *78*(19), 197–204.

Kagan, Y. Y. (2002). Seismic moment distribution revisited: I. Statistical results. *Geophysical Journal International*, *148*, 520–541. https://doi.org/10.1046/j.1365-246x.2002.01594.x

Kelley, D. S., Delaney, J. R., & Juniper, S. K. (2014). Establishing a new era of submarine volcanic observatories: Cabling axial seamount and the endeavour segment of the Juan de Fuca Ridge. *Marine Geology 50th Anniversary Special*, *352*, 426–450. https://doi.org/10.1016/j.margeo.2014.03.010

Kowalik, Z., Horrillo, J., Knight, W., & Logan, T. (2008). Kuril Islands tsunami of November 2006: 1. Impact at Crescent City by distant scattering. *Journal of Geophysical Research*, *113*, C01020. https://doi.org/10.1029/2007JC004402

Lander, J. F., Whiteside, L. S., & Lockridge, P. A. (2003). Two decades of global tsunamis, 1982-2002. *Science of Tsunami Hazards, Honolulu, Hawaii, USA*, *21*(1), 3–82.

Lobkovsky, L. I., Rabinovich, A. B., Kulikov, E. A., Ivashchenko, A. I., Fine, I. V., Thomson, R. E., et al. (2009). The Kuril earthquakes and tsunamis of November 15, 2006, and January 13, 2007: Observations, analysis, and numerical modeling. *Oceanology*, *49*(2), 166–181. https://doi.org/10.1134/S0001437009020027

National Geophysical Data Center/World Data Service: NCEI/WDS Global Historical Tsunami Database. NOAA National Centers for Environmental Information. doi:https://doi.org/10.7289/V5PN93H7 [last accessed on December 20, 2019]

Nooner, S. L., & Chadwick, W. W. Jr. (2009). Volcanic inflation measured in the caldera of axial seamount: Implications for magma supply and future eruptions. *Geochemistry, Geophysics, Geosystems*, *10*, Q02002. https://doi.org/10.1029/2008GC002315

Nooner, S. L., & Chadwick, W. W. Jr. (2016). Inflation-predictable behavior and co-eruption deformation at axial seamount. *Science*, *354*(6318), 1399–1403. https://doi.org/10.1126/science.aah4666

Pawlowicz, R., Beardsley, B., & Lentz, S. (2002). Classical tidal harmonic analysis including error estimating in MATLAB using T_TIDE. *Computers and Geosciences*, *28*, 929–937. https://doi.org/10.1016/S0098-3004(02)00013-4

Rabinovich, A., & Eblé, M. (2015). Deep-ocean measurements of tsunami waves. *Pure and Applied Geophysics*, *172*(12), 3281–3312. https://doi.org/10.1007/s00024-015-1058-1

Ross, Z. E., Trugman, D. T., Hauksson, E., & Shearer, P. M. (2019). Searching for hidden earthquakes in Southern California. *Science*, *364*, 767–770.

Snodgrass, F. E. (1969). Study of ocean waves, 10-5 to 1 Hz, Survey Paper No. 8, Horace Lamb Centre, Flinders, University of Australia, 41 pp.

Thomson, R. E., & Emery, W. J. (2014). *Data Analysis Methods in Physical Oceanography*, (3nd ed.p. 716). Amsterdam, London, New York: Elsevier Science.